

Dynamical properties of collective excitations in twisted bilayer grapheneGaopei Pan^{1,2}, Xu Zhang³, Heqiu Li^{4,5}, Kai Sun^{4,*} and Zi Yang Meng^{3,†}¹*Beijing National Laboratory for Condensed Matter Physics and Institute of Physics, Chinese Academy of Sciences, Beijing 100190, China*²*School of Physical Sciences, University of Chinese Academy of Sciences, Beijing 100190, China*³*Department of Physics and HKU-UCAS Joint Institute of Theoretical and Computational Physics, The University of Hong Kong, Pokfulam Road, Hong Kong SAR, China*⁴*Department of Physics, University of Michigan, Ann Arbor, Michigan 48109, USA*⁵*Department of Physics, University of Toronto, Toronto, Ontario, Canada M5S 1A7*

(Received 1 September 2021; revised 11 January 2022; accepted 28 February 2022; published 16 March 2022)

Employing the recently developed momentum-space quantum Monte Carlo scheme, we study the dynamic response of single-particle and collective excitations in realistic continuum models of twisted bilayer graphene. At charge neutrality with small flat-band dispersion, this unbiased numerical method reveals single-particle spectra and collective excitations at finite temperature. Single-particle spectra indicate that repulsive interactions push the fermion spectral weight away from the Fermi energy and open up an insulating gap. The spectra of collective excitations suggest an approximate valley SU(2) symmetry. At low energy, long-lived valley waves are observed, which resemble spin waves of Heisenberg ferromagnetism. At high energy, these sharp modes quickly become overdamped, when their energy reaches the fermion particle-hole continuum.

DOI: [10.1103/PhysRevB.105.L121110](https://doi.org/10.1103/PhysRevB.105.L121110)

Introduction. To understand the rich physics in twisted bilayer graphene (TBG), as well as the mechanism that governs this novel quantum system, a crucial step is to identify the ground state and to characterize the associated low-energy excitations [1–23]. Recently, many new insights have been obtained using real-space effective model analysis and large-scale numerical simulations [e.g., quantum Monte Carlo and density matrix renormalization group (DMRG)] [24–30], which indicate that even at integer fillings, correlation effects give rise to a very rich phase diagram with a variety of competing quantum phases. A key advantage of this approach is that these lattice models can be easily incorporated with well-established numerical techniques, but it remains a challenge to determine the effective control parameters utilized in these models from first principles. Another parallel approach utilizes continuum models with flat bands and fragile topology [31–33], where Coulomb interactions and first-principles material parameters can be easily incorporated. In this approach, a key theoretical challenge is to handle the strong Coulomb interactions. In certain special limits, exact solutions exist due to emergent high symmetry [34]. For realistic material parameters away from these special cases, Hartree-Fock mean-field and DMRG calculations suggest that the ground state is likely to be an intervalley coherent (IVC) state [20–23,35–38], which mixes electron states from the two opposite valleys and breaks the $U_v(1)$ valley charge conservation. There have been many studies about symmetry-breaking ground states of

such systems [36,39–42], while finite temperature results and the collective excitation are matters of widespread concern. To fully understand such a complex many-body system, unbiased numerical methodology, which can solve such correlated problems efficiently and accurately, is in great need.

In this Letter, we utilize the momentum-space quantum Monte Carlo (QMC) method [43–46] to achieve this objective. The implementation of this method in continuum models of TBG has been developed recently [45,46], but a dynamic response, in particular the spectral information of the collective excitations, has not yet been obtained. Here, we employ the momentum-space QMC method, accompanied by the stochastic analytic (SAC) continuation scheme [47–53], to compute the spectra of both single-particle and particle-hole excitations. We find that, at the charge neutrality point (CNP), the IVC state is the leading instability, with strong competition from the VP state. More interestingly, although the valley SU(2) symmetry is broken explicitly when control parameters take realistic values (with a kinetic term), the dynamic response of particle-hole excitations still exhibits an approximate SU(2) symmetry. At low energy, long-lived valley waves are observed in close analogy to spin waves of a Heisenberg ferromagnet, and these modes become overdamped as their energy reaches the particle-hole continuum. These results reveal a complex dynamic response in TBG and provide a foundation for the study of other intriguing physics at and away from charge neutrality, such as the mechanism of superconductivity and its possible topological origin [18,22,23,54].

Model and method. In this study, we utilize the continuum model of a TBG flat band introduced in Refs. [1–6]. In the plane-wave basis, the single-particle Hamiltonian can be

*sunkai@umich.edu

†zymeng@hku.hk

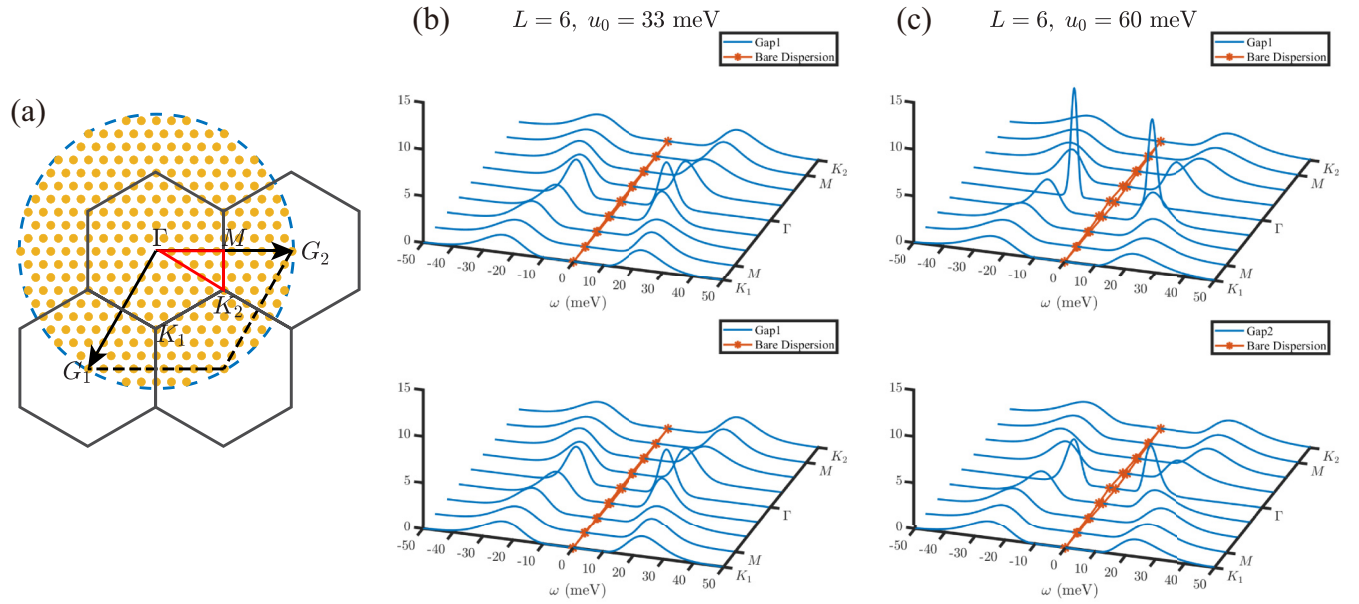


FIG. 1. (a) The moiré Brillouin zones (mBZs) at one valley. The red solid line marks the high-symmetry path Γ - M - K_1 (K_2)- Γ . \mathbf{G}_1 and \mathbf{G}_2 are the reciprocal lattice vectors of the mBZ. Yellow dots mark the possible momentum transfer in QMC simulations, $\mathbf{q} + \mathbf{G}$, and the blue dashed circle is the momentum-space cutoff. Because the form factor decays exponentially with \mathbf{G} [34], scatterings with momentum transfer larger than this cutoff are ignored. Here, we show a 9×9 mesh in the mBZ, with 300 allowed momentum transfers. In (b) and (c), blue lines are single-particle spectra of $L = 6$, $T = 0.667$ meV, $u_0 = 33$ and 60 meV (realistic case [36,55–58]), respectively, obtained from the momentum-space QMC with analytic continuation. The red stars and lines indicate the bare dispersions of H_0 , which is the kinetic energy in our model in Eq. (3).

written as

$$\begin{aligned}
 H_{0,\mathbf{k},\mathbf{k}'}^\tau &= \delta_{\mathbf{k},\mathbf{k}'} \begin{pmatrix} -\hbar v_F (\mathbf{k} - \mathbf{K}_1^\tau) \cdot \boldsymbol{\sigma}^\tau & U_0 \\ U_0^\dagger & -\hbar v_F (\mathbf{k} - \mathbf{K}_2^\tau) \cdot \boldsymbol{\sigma}^\tau \end{pmatrix} \\
 &+ \begin{pmatrix} 0 & U_1^\tau \delta_{\mathbf{k},\mathbf{k}'-\tau\mathbf{G}_1} \\ U_1^{\tau\dagger} \delta_{\mathbf{k},\mathbf{k}'+\tau\mathbf{G}_1} & 0 \end{pmatrix} \\
 &+ \begin{pmatrix} 0 & U_2^\tau \delta_{\mathbf{k},\mathbf{k}'-\tau(\mathbf{G}_1+\mathbf{G}_2)} \\ U_2^{\tau\dagger} \delta_{\mathbf{k},\mathbf{k}'+\tau(\mathbf{G}_1+\mathbf{G}_2)} & 0 \end{pmatrix}, \quad (1)
 \end{aligned}$$

where v_F is the Dirac velocity, $\tau = \pm$ is the valley index, and $\boldsymbol{\sigma}^\tau = (\tau\sigma_x, \sigma_y)$ defines the A,B sublattices of the monolayer graphene. The $\mathbf{K}_{1,2}^\tau$ are the corresponding Dirac points of the bottom and top layers, which are twisted by angles $\mp\frac{\theta}{2}$, respectively. As shown in Fig. 1(a), $\mathbf{G}_1 = (-\frac{2\pi}{\sqrt{3}L_M}, -\frac{2\pi}{L_M})$ and $\mathbf{G}_2 = (\frac{4\pi}{\sqrt{3}L_M}, 0)$ are reciprocal lattice vectors of the moiré Brillouin zone (mBZ), with $L_M = a_0/[2 \sin(\theta/2)]$ and $a_0 = 0.246$ nm. Interlayer tunnelings are described by $U_0 = \begin{pmatrix} u_0 & u_1 \\ u_1 & u_0 \end{pmatrix}$, $U_1^\tau = \begin{pmatrix} u_0 & u_1 e^{-\tau\frac{2\pi}{3}i} \\ u_1 e^{\tau\frac{2\pi}{3}i} & u_0 \end{pmatrix}$, and $U_2^\tau = \begin{pmatrix} u_0 & u_1 e^{\tau\frac{2\pi}{3}i} \\ u_1 e^{-\tau\frac{2\pi}{3}i} & u_0 \end{pmatrix}$, where u_0 and u_1 are the intra- and intersublattice interlayer tunneling amplitudes. In this Letter, we set $\hbar v_F/a_0 = 2377.45$ meV, $\theta = 1.08^\circ$, and $u_1 = 110$ meV, which means the moiré bands are completely flat at the chiral limit $u_0 = 0$ [55–58].

We then project the charge-density operator at $\mathbf{q} + \mathbf{G}$ to the nearly flat bands relative to the filling of

CNP,

$$\begin{aligned}
 \delta\rho_{\mathbf{q}+\mathbf{G}} &= \sum_{\mathbf{k} \in \text{mBZ}, m_1, m_2, \tau, s} \lambda_{m_1, m_2, \tau}(\mathbf{k}, \mathbf{k} + \mathbf{q} + \mathbf{G}) \\
 &\times \left(d_{\mathbf{k}, m_1, \tau, s}^\dagger d_{\mathbf{k}+\mathbf{q}, m_2, \tau, s} - \frac{1}{2} \delta_{\mathbf{q}, 0} \delta_{m_1, m_2} \right) \\
 &= (\delta\rho_{-\mathbf{q}-\mathbf{G}})^\dagger, \quad (2)
 \end{aligned}$$

where $d_{\mathbf{k}, m, \tau, s}^\dagger$ is the creation operator for a Bloch eigenstate, $|u_{\mathbf{k}, m, \tau, s}\rangle$, with m, s, τ the band, spin, and valley indices. The form factor is defined as $\lambda_{m_1, m_2, \tau}(\mathbf{k}, \mathbf{k} + \mathbf{q} + \mathbf{G}) \equiv \langle u_{\mathbf{k}, m_1, \tau} | u_{\mathbf{k}+\mathbf{q}+\mathbf{G}, m_2, \tau} \rangle$. As shown in Fig. 1(a), $\mathbf{q} \in \text{mBZ}$ and $\mathbf{q} + \mathbf{G}$ represents a vector in extended mBZ, with $\mathbf{G} = n_1 \mathbf{G}_1 + n_2 \mathbf{G}_2$, $n_1, n_2 \in \mathbb{Z}$ [56,57]. After projecting to the flat band, the Hamiltonian reads

$$\begin{aligned}
 H &= H_0 + H_{\text{int}}, \\
 H_0 &= \sum_{m=\pm 1} \sum_{\mathbf{k}, \tau, s} \epsilon_{m, \tau}(\mathbf{k}) d_{\mathbf{k}, m, \tau, s}^\dagger d_{\mathbf{k}, m, \tau, s}, \quad (3) \\
 H_{\text{int}} &= \frac{1}{2\Omega} \sum_{\mathbf{q}, \mathbf{G}, |\mathbf{q}+\mathbf{G}| \neq 0} V(\mathbf{q} + \mathbf{G}) \delta\rho_{\mathbf{q}+\mathbf{G}} \delta\rho_{-\mathbf{q}-\mathbf{G}},
 \end{aligned}$$

where $\epsilon_{m, \tau}(\mathbf{k})$ is the eigenvalue of the continuum model in Eq. (1). We define the long-ranged single-gate (screened) Coulomb potential: $V(\mathbf{q}) = \frac{e^2}{4\pi\epsilon} \int d^2\mathbf{r} \left(\frac{1}{r} - \frac{1}{\sqrt{r^2+d^2}} \right) e^{i\mathbf{q}\cdot\mathbf{r}} = \frac{e^2}{2\epsilon} \frac{1}{q} (1 - e^{-qd})$. Here, $\frac{d}{2}$ is the distance between the graphene layer and single gate, with $d = 40$ nm and $\epsilon = 7\epsilon_0$. The volume $\Omega = N_{\mathbf{k}} \frac{\sqrt{3}}{2} L_M^2$ with $N_{\mathbf{k}}$ being the number of momentum points in a mBZ (e.g., $N_{\mathbf{k}} = 81$ for a 9×9

mesh). We choose the bare dispersion, as it is shown in Ref. [37] that the renormalization from a remote band has been considered in our form of interaction, while it is worth noticing in Refs. [35,38,42] that the mean-field contribution of the remote band interaction from the flat band is removed. Whether this remote band interaction is strong enough to change the parameter of the moiré potential obviously is under debate. In our work, we choose the case where the flat-band approximation is reasonable to carry out our simulation.

The problem associated with the projected Coulomb interaction is solved via a discrete Hubbard-Stratonovich transformation [28,45,59,60], $e^{\alpha\hat{\rho}^2} = \frac{1}{4} \sum_{l=\pm 1, \pm 2} \gamma(l) e^{\sqrt{\alpha\eta}(l)\hat{\rho}} + O(\alpha^4)$ [details are shown in Sec. I of the Supplemental Material (SM) [61]].

Exact ground states in the flat-band limit. When the kinetic energy is ignored (i.e., the flat-band limit), the TBG Hamiltonian at charge neutrality has an emergent $U(4)$ symmetry and ground states can be obtained exactly [34,35,46,62]. To see the exact solution, one just needs to realize that the valley-polarized state, with all electrons in one valley, is a zero-energy eigenstate of H_{int} . Because H_{int} is semipositive definite, this must be a ground state. In addition, any $U(4)$ transformation of this ground state is also a degenerate ground state, including the VP, IVC, and spin-polarized states, as well as many other degenerate states. For simplicity, in this Letter, we will focus only on the VP and IVC states.

We define the VP and IVC order parameters as $\mathcal{O}_a(\mathbf{q}, \tau) \equiv \sum_k d_{k+\mathbf{q}}^\dagger(\tau) M_a d_k(\tau)$, with $M_a = \tau_z \eta_0$ (η_0 for the band index) for VP and $M_a = \tau_x \eta_y$ or $\tau_y \eta_x$ for the IVC states [20,34,35,40,46]. It is straightforward to verify that at $q = 0$, these three order parameters obey the commutation relations $[\mathcal{O}_a, \mathcal{O}_b] = i\epsilon_{a,b,c} \mathcal{O}_c$ and they all commute with the interaction Hamiltonian $[\mathcal{O}_a, H_{\text{int}}] = 0$. Thus, they generate a $SU(2)$ symmetry group, a subgroup of the full $U(4)$ symmetry. In the ordered phase, the nonzero expectation value of these order parameters spontaneously breaks this $SU(2)$ symmetry, resulting in spin-wave-like gapless Goldstone modes, i.e., valley waves. The same as ferromagnetism, such valley waves have a quadratic dispersion $\omega \propto k^2$ at low energy.

As for single-particle excitations, all these degenerate ground states are insulators with a gap proportional to the interaction strength. In the flat-band limit, a single-particle Green's function can be calculated exactly at $T = 0$ [34]. Despite the strong Coulomb repulsion, electrons/holes exhibit free-fermion-like behavior, where the Green's function shows four fermion bands with zero damping: two conduction (valence) bands above (below) the Fermi energy.

In a real TBG, away from the flat-band limit, this $SU(2)$ symmetry is explicitly broken by the kinetic energy down to Z_2 (valley) and $U_v(1)$ (valley charge conservation), lifting the degeneracy between the VP and IVC states. Here, an IVC (VP) state breaks the continuous $U(1)$ (discrete Z_2) symmetry, and dynamics fluctuations in VP and IVC states shall exhibit different behaviors. However, if the kinetic energy term is small (i.e., small bandwidth), an approximate $SU(2)$ symmetry may survive, and qualitative features may still resemble the flat-band limit. The momentum-space QMC technique offers a probe to directly visualize the breaking

of the $SU(2)$ symmetry as well as the remnant approximate symmetry.

Results and analysis. In a previous work [45], we have shown that H_{int} acquires a correlated insulator ground state at CNP. In this study, we added the kinetic term H_0 and carried out the simulations at $u_0 = 33$ and 60 meV with 6×6 and 9×9 momentum meshes. Here, $u_0 = 60$ meV is a realistic case [36,55–58] which leads to a bandwidth of 1.08 meV, and $u_0 = 33$ meV is a case between the realistic one and chiral limit. The single-particle spectra are shown in Figs. 1(b) and 1(c). The bare (noninteracting) dispersions are depicted as red stars. At low temperature, for both $u_0 = 33$ and 60 meV, interactions push the fermion states away from the Fermi energy, resulting in an interaction-driven band gap of ~ 20 meV, with magnitudes larger than that of the bare bandwidth. Although we are using realistic parameters away from the flat-band limit, as shown in Figs. 2(c) and 2(d), the peak of the single-particle spectra agrees nicely with the solution of the flat-band limit [34], indicating that the system is not far from the exactly solvable limit. As for the width of the peak, due to the finite temperature and the presence of kinetic energy, fermions here exhibit some damping of the order 10 meV, which is significantly larger than T and the bandwidth of the bare dispersion. This is in contrast to the exactly solvable limit at $T = 0$ where the damping vanishes.

The next question is to reveal the symmetry-breaking channels of this insulating state. The proposed symmetry-breaking states at the CNP, based on a Hartree-Fock mean-field analysis, are gradually pointing towards the IVC and VP states [35,36,39,40]. Here, we calculate their corresponding (dynamical) correlation

$$S_a(\mathbf{q}, \tau) \equiv \frac{1}{N_k^2} \langle \mathcal{O}_a(-\mathbf{q}, \tau) \mathcal{O}_a(\mathbf{q}, 0) \rangle, \quad (4)$$

where \mathcal{O}_a is the order parameter of the VP or IVC state defined early on. For static properties, we calculate the equal-time correlation at imaginary time $\tau = 0$. To obtain a dynamic response, the time-dependent $S_a(\mathbf{q}, \tau)$ is calculated at $\tau \in [0, \beta]$, followed by the stochastic analytic continuation (SAC) [47–52,63–68] to obtain the real frequency spectra [61].

The static order parameters are presented in Figs. 2(a) and 2(b), where we calculate $S(\mathbf{q} = \Gamma, \tau = 0)$, the squares of the order parameter, for IVC and VP as a function of temperature. Without the kinetic energy ($H = H_{\text{int}}$), IVC and VP share an identical susceptibility, which reflects the $SU(2)$ symmetry of the flat-band limit. Once the kinetic energy is included [“with kin” in Figs. 2(a) and 2(b)], this degeneracy is lifted. At $u_0 = 33$ meV, a small splitting between IVC and VP correlation functions is observed. The splitting becomes more significant when u_0 reaches 60 meV, closer to the realistic case [69,70], with IVC being the more favored ground state. It is worthwhile to note that when the system size goes from 6×6 to 9×9 , the IVC order $S(\mathbf{q} = \Gamma)$ does not change, whereas the VP $S(\mathbf{q} = \Gamma)$ decreases as the system size increases. One shall also notice that although the degeneracy between IVC and VP is lifted, both correlation functions grow at low T , indicating that the competition between IVC and VP remains strong and there is no completely dominant symmetry-breaking channel [40].

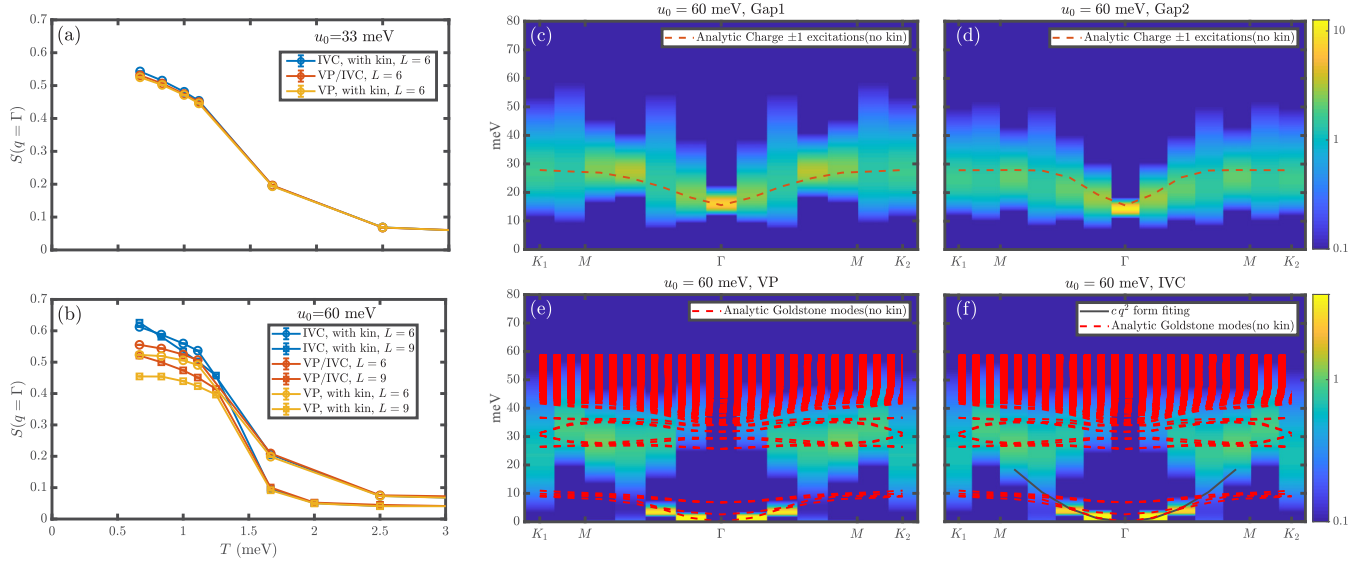


FIG. 2. (a) $S(\mathbf{q} = \Gamma, \tau = 0)$, the squares of order parameters, for VP and IVC at $u_0 = 33$ meV and $L = 6$, as a function of temperature. (b) The same quantity at $u_0 = 60$ meV with both $L = 6$ and 9 . When kinetic energy is ignored, the two order parameters are degenerate due to an emergent $SU(2)$ [$U(4)$] symmetry. When the kinetic energy is taken into account (“with kin”), which breaks the symmetry, this degeneracy is lifted. At $u_0 = 33$ meV, the splitting between VP and IVC is weak. This splitting becomes more pronounced at $u_0 = 60$ meV, indicating that IVC is more favored at low temperatures in comparison to VP, although the competition between these two symmetry-breaking channels remains. (c) and (d) Single-particle spectra at $T = 0.667$ meV, $u_0 = 60$ meV, and $L = 9$, which shows an insulating gap ~ 10 meV. The dashed lines are the analytic computation of the single-particle dispersion at the flat-band limit following Ref. [34]. (e) and (f) Dynamical spectra of VP and IVC with the same parameters. Sharp and ferromagneticlike valley waves are observed in both channels near $\mathbf{q} = \Gamma$ and a fit of $c q^2$ gives rise to $c = 31.32 \pm 0.03$ meV/ k_θ^2 [black solid line in (f)]. At the energy scale of twice the single-particle gap, ~ 20 meV, valley waves are overdamped into the particle-hole continuum. The dashed lines are the analytic computation of the Goldstone mode at the flat-band limit following Ref. [34].

In addition to static correlations, we also compute the dynamic correlations of IVC and VP as defined in Eq. (4) and their spectra with a system size of 9×9 for the realistic case with the kinetic energy at $u_0 = 60$ meV at low temperature $T = 0.667$ meV, much lower than the scale of the single-particle gap. The results are shown in Figs. 2(e) and 2(f), with Figs. 2(c) and 2(d) the associated single-particle spectra. The dashed lines mark the single-particle dispersion and Goldstone modes when the kinetic energy is ignored [34]. Measured from $\omega = 0$, the single-particle gap is of size ~ 10 meV and both the VP and IVC spectra develop a clear and sharp valley wave dispersion at low energy near Γ . Remarkably, although the static susceptibility indicates that the $SU(2)$ symmetry has been explicitly broken at $u_0 = 60$ meV and the degeneracy between IVC and VP is lifted [Fig. 2(b)], the IVC and VP spectra are almost identical and are strikingly similar to the flat-band limit [34,71]. These sharp Goldstone-like modes are in strong analogy to $SU(2)$ ferromagnetic Goldstone modes with $\omega \propto c q^2$ and $c = 31.32 \pm 0.03$ meV/ k_θ^2 [where $k_\theta = 8\pi \sin(\theta/2)/(3a_0)$ and the lattice constant of the monolayer graphene $a_0 = 0.246$ nm], indicating an approximate $SU(2)$ symmetry survives in our model. It is worthwhile to highlight that this $SU(2)$ approximate symmetry is not an exact symmetry and it breaks at low energy. Thus, at very small q and ω , this magnonlike excitation will exhibit a linear dispersion $\omega \propto q$, due to the broken $SU(2)$ symmetry [20]. For our study, because this $SU(2)$ symmetry breaking is really weak, such a linear dispersion is not visible in the QMC data.

One other interesting feature of these valley waves is that above the energy scale of ~ 20 meV, the sharp collective excitations become heavily damped, which is not seen in the analytical solution [dashed line in Figs. 2(e) and 2(f)]. The analytical solutions (without kinetic energy) are only consistent with QMC results (with kinetic energy) at the low-energy mode near the Γ point, which means that our results are beyond the mean-field type of calculations. The damping of collective modes has two origins: (1) scattering between collective modes and (2) damping due to the fermion particle-hole continuum. The second damping channel arises for energy larger than twice the fermion gap, and thus is responsible for the overdamped features at energies above 20 meV shown in Figs. 2(e) and 2(f). This is in strong analogy to the damping of ferromagnetic spin excitations in the graphene nanoribbons, where the flat band gives rise to the ferromagnetic long-range order but the spin waves become overdamped in the particle-hole continuum [71–73].

Discussion and outlook. The quantum dynamics of collective excitations holds the key to the understanding of many-body effects in twisted bilayer graphene and other quantum moiré systems. This study suggests that the momentum-space QMC method offers a powerful tool to tackle this problem. In particular, the spectral function obtained via this unbiased method offers a bridge to directly connect theoretical studies with experimental measurements, especially spectroscopy methods, such as inelastic light or neutron scattering

and tunneling spectroscopy, making it possible to compare measurements in experiments and large-scale quantum simulations at the quantitative level.

Acknowledgments. We are indebted to Yi Zhang for the help in the form factor tables. We thank Tianyu Qiao, Jian Kang, Jianpeng Liu, and Xi Dai for stimulating discussions. G.P.P., X.Z., and Z.Y.M. acknowledge support from the RGC of Hong Kong SAR of China (Grant Nos. 17303019, 17301420, 17301721, and AoE/P701/20), the Strategic Priority Research Program of the Chinese Academy of Sciences (Grant

No. XDB33000000), the K. C. Wong Education Foundation (Grant No. GJTD-2020-01) and the Seed Funding “QuantumInspired explainable-AI” at the HKU-TCL Joint Research Centre for Artificial Intelligence. H.L. and K.S. acknowledge support through NSF Grant No. NSF-EFMA-1741618. We thank the Computational Initiative at the Faculty of Science and the Information Technology Services at the University of Hong Kong and the Tianhe platforms at the National Supercomputer Center in Guangzhou for their technical support and generous allocation of CPU time.

-
- [1] G. Trambly de Laissardière, D. Mayou, and L. Magaud, Localization of Dirac electrons in rotated graphene bilayers, *Nano Lett.* **10**, 804 (2010).
- [2] G. Trambly de Laissardière, D. Mayou, and L. Magaud, Numerical studies of confined states in rotated bilayers of graphene, *Phys. Rev. B* **86**, 125413 (2012).
- [3] R. Bistritzer and A. H. MacDonald, Moiré bands in twisted double-layer graphene, *Proc. Natl. Acad. Sci. USA* **108**, 12233 (2011).
- [4] A. Rozhkov, A. Sboychakov, A. Rakhmanov, and F. Nori, Electronic properties of graphene-based bilayer systems, *Phys. Rep.* **648**, 1 (2016).
- [5] J. M. B. Lopes dos Santos, N. M. R. Peres, and A. H. Castro Neto, Graphene Bilayer with a Twist: Electronic Structure, *Phys. Rev. Lett.* **99**, 256802 (2007).
- [6] J. M. B. Lopes dos Santos, N. M. R. Peres, and A. H. Castro Neto, Continuum model of the twisted graphene bilayer, *Phys. Rev. B* **86**, 155449 (2012).
- [7] Y. Cao, V. Fatemi, S. Fang, K. Watanabe, T. Taniguchi, E. Kaxiras, and P. Jarillo-Herrero, Unconventional superconductivity in magic-angle graphene superlattices, *Nature (London)* **556**, 43 (2018).
- [8] Y. Cao, V. Fatemi, A. Demir, S. Fang, S. L. Tomarken, J. Y. Luo, J. D. Sanchez-Yamagishi, K. Watanabe, T. Taniguchi, E. Kaxiras *et al.*, Correlated insulator behaviour at half-filling in magic-angle graphene superlattices, *Nature (London)* **556**, 80 (2018).
- [9] G. Chen, A. L. Sharpe, E. J. Fox, Y.-H. Zhang, S. Wang, L. Jiang, B. Lyu, H. Li, K. Watanabe, T. Taniguchi *et al.*, Tunable correlated Chern insulator and ferromagnetism in a moiré superlattice, *Nature (London)* **579**, 56 (2020).
- [10] A. Kerelsky, L. J. McGilly, D. M. Kennes, L. Xian, M. Yankowitz, S. Chen, K. Watanabe, T. Taniguchi, J. Hone, C. Dean *et al.*, Maximized electron interactions at the magic angle in twisted bilayer graphene, *Nature (London)* **572**, 95 (2019).
- [11] S. L. Tomarken, Y. Cao, A. Demir, K. Watanabe, T. Taniguchi, P. Jarillo-Herrero, and R. C. Ashoori, Electronic Compressibility of Magic-Angle Graphene Superlattices, *Phys. Rev. Lett.* **123**, 046601 (2019).
- [12] X. Lu, P. Stepanov, W. Yang, M. Xie, M. A. Aamir, I. Das, C. Urgell, K. Watanabe, T. Taniguchi, G. Zhang *et al.*, Superconductors, orbital magnets and correlated states in magic-angle bilayer graphene, *Nature (London)* **574**, 653 (2019).
- [13] Y. Xie, B. Lian, B. Jäck, X. Liu, C.-L. Chiu, K. Watanabe, T. Taniguchi, B. A. Bernevig, and A. Yazdani, Spectroscopic signatures of many-body correlations in magic-angle twisted bilayer graphene, *Nature (London)* **572**, 101 (2019).
- [14] C. Shen, Y. Chu, Q. Wu, N. Li, S. Wang, Y. Zhao, J. Tang, J. Liu, J. Tian, K. Watanabe, T. Taniguchi, R. Yang, Z. Y. Meng, D. Shi, O. V. Yazyev, and G. Zhang, Correlated states in twisted double bilayer graphene, *Nat. Phys.* **16**, 520 (2020).
- [15] K. P. Nuckolls, M. Oh, D. Wong, B. Lian, K. Watanabe, T. Taniguchi, B. A. Bernevig, and A. Yazdani, Strongly correlated Chern insulators in magic-angle twisted bilayer graphene, *Nature (London)* **588**, 610 (2020).
- [16] A. T. Pierce, Y. Xie, J. M. Park, E. Khalaf, S. H. Lee, Y. Cao, D. E. Parker, P. R. Forrester, S. Chen, K. Watanabe, T. Taniguchi, A. Vishwanath, P. Jarillo-Herrero, and A. Yacoby, Unconventional sequence of correlated Chern insulators in magic-angle twisted bilayer graphene, *Nat. Phys.* **17**, 1210 (2021).
- [17] S. Moriyama, Y. Morita, K. Komatsu, K. Endo, T. Iwasaki, S. Nakaharai, Y. Noguchi, Y. Wakayama, E. Watanabe, D. Tsuya, K. Watanabe, and T. Taniguchi, Observation of superconductivity in bilayer graphene/hexagonal boron nitride superlattices, [arXiv:1901.09356](https://arxiv.org/abs/1901.09356).
- [18] A. Rozen, J. M. Park, U. Zondiner, Y. Cao, D. Rodan-Legrain, T. Taniguchi, K. Watanabe, Y. Oreg, A. Stern, E. Berg, P. Jarillo-Herrero, and S. Ilani, Entropic evidence for a Pomeranchuk effect in magic-angle graphene, *Nature (London)* **592**, 214 (2021).
- [19] X. Liu, C.-L. Chiu, J. Y. Lee, G. Farahi, K. Watanabe, T. Taniguchi, A. Vishwanath, and A. Yazdani, Spectroscopy of a tunable moiré system with a correlated and topological flat band, *Nat. Commun.* **12**, 2732 (2021).
- [20] E. Khalaf, N. Bultinck, A. Vishwanath, and M. P. Zaletel, Soft modes in magic angle twisted bilayer graphene, [arXiv:2009.14827](https://arxiv.org/abs/2009.14827).
- [21] T. Soejima, D. E. Parker, N. Bultinck, J. Hauschild, and M. P. Zaletel, Efficient simulation of moiré materials using the density matrix renormalization group, *Phys. Rev. B* **102**, 205111 (2020).
- [22] E. Khalaf, S. Chatterjee, N. Bultinck, M. P. Zaletel, and A. Vishwanath, Charged skyrmions and topological origin of superconductivity in magic-angle graphene, *Sci. Adv.* **7**, [doi:10.1126/sciadv.abf5299](https://doi.org/10.1126/sciadv.abf5299) (2021).
- [23] S. Chatterjee, M. Ippoliti, and M. P. Zaletel, Skyrmion superconductivity: DMRG evidence for a topological route to superconductivity, [arXiv:2010.01144](https://arxiv.org/abs/2010.01144).
- [24] M. Koshino, N. F. Q. Yuan, T. Koretsune, M. Ochi, K. Kuroki, and L. Fu, Maximally Localized Wannier Orbitals and the

- Extended Hubbard Model for Twisted Bilayer Graphene, *Phys. Rev. X* **8**, 031087 (2018).
- [25] J. Kang and O. Vafek, Symmetry, Maximally Localized Wannier States, and a Low-Energy Model for Twisted Bilayer Graphene Narrow Bands, *Phys. Rev. X* **8**, 031088 (2018).
- [26] X. Y. Xu, K. T. Law, and P. A. Lee, Kekulé valence bond order in an extended Hubbard model on the honeycomb lattice with possible applications to twisted bilayer graphene, *Phys. Rev. B* **98**, 121406(R) (2018).
- [27] J. Kang and O. Vafek, Strong Coupling Phases of Partially Filled Twisted Bilayer Graphene Narrow Bands, *Phys. Rev. Lett.* **122**, 246401 (2019).
- [28] Y. D. Liao, J. Kang, C. N. Breið, X. Y. Xu, H.-Q. Wu, B. M. Andersen, R. M. Fernandes, and Z. Y. Meng, Correlation-Induced Insulating Topological Phases at Charge Neutrality in Twisted Bilayer Graphene, *Phys. Rev. X* **11**, 011014 (2021).
- [29] Y.-D. Liao, X.-Y. Xu, Z.-Y. Meng, and J. Kang, Correlated insulating phases in the twisted bilayer graphene, *Chin. Phys. B* **30**, 017305 (2021).
- [30] B.-B. Chen, Y. D. Liao, Z. Chen, O. Vafek, J. Kang, W. Li, and Z. Y. Meng, Realization of topological Mott insulator in a twisted bilayer graphene lattice model, *Nat. Commun.* **12**, 5480 (2021).
- [31] H. C. Po, L. Zou, A. Vishwanath, and T. Senthil, Origin of Mott Insulating Behavior and Superconductivity in Twisted Bilayer Graphene, *Phys. Rev. X* **8**, 031089 (2018).
- [32] H. C. Po, H. Watanabe, and A. Vishwanath, Fragile Topology and Wannier Obstructions, *Phys. Rev. Lett.* **121**, 126402 (2018).
- [33] H. C. Po, L. Zou, T. Senthil, and A. Vishwanath, Faithful tight-binding models and fragile topology of magic-angle bilayer graphene, *Phys. Rev. B* **99**, 195455 (2019).
- [34] B. A. Bernevig, B. Lian, A. Cowsik, F. Xie, N. Regnault, and Z.-D. Song, Twisted bilayer graphene. V. Exact analytic many-body excitations in Coulomb Hamiltonians: Charge gap, Goldstone modes, and absence of Cooper pairing, *Phys. Rev. B* **103**, 205415 (2021).
- [35] N. Bultinck, E. Khalaf, S. Liu, S. Chatterjee, A. Vishwanath, and M. P. Zaletel, Ground State and Hidden Symmetry of Magic-Angle Graphene at Even Integer Filling, *Phys. Rev. X* **10**, 031034 (2020).
- [36] Y. Zhang, K. Jiang, Z. Wang, and F. Zhang, Correlated insulating phases of twisted bilayer graphene at commensurate filling fractions: A Hartree-Fock study, *Phys. Rev. B* **102**, 035136 (2020).
- [37] O. Vafek and J. Kang, Renormalization Group Study of Hidden Symmetry in Twisted Bilayer Graphene with Coulomb Interactions, *Phys. Rev. Lett.* **125**, 257602 (2020).
- [38] D. E. Parker, T. Soejima, J. Hauschild, M. P. Zaletel, and N. Bultinck, Strain-Induced Quantum Phase Transitions in Magic-Angle Graphene, *Phys. Rev. Lett.* **127**, 027601 (2021).
- [39] J. Liu, J. Liu, and X. Dai, Pseudo Landau level representation of twisted bilayer graphene: Band topology and implications on the correlated insulating phase, *Phys. Rev. B* **99**, 155415 (2019).
- [40] J. Liu and X. Dai, Theories for the correlated insulating states and quantum anomalous Hall effect phenomena in twisted bilayer graphene, *Phys. Rev. B* **103**, 035427 (2021).
- [41] B. Lian, Z.-D. Song, N. Regnault, D. K. Efetov, A. Yazdani, and B. A. Bernevig, Twisted bilayer graphene. IV. Exact insulator ground states and phase diagram, *Phys. Rev. B* **103**, 205414 (2021).
- [42] Y. H. Kwan, G. Wagner, T. Soejima, M. P. Zaletel, S. H. Simon, S. A. Parameswaran, and N. Bultinck, Kekulé Spiral Order at All Nonzero Integer Fillings in Twisted Bilayer Graphene, *Phys. Rev. X* **11**, 041063 (2021).
- [43] M. Ippoliti, R. S. K. Mong, F. F. Assaad, and M. P. Zaletel, Half-filled Landau levels: A continuum and sign-free regularization for three-dimensional quantum critical points, *Phys. Rev. B* **98**, 235108 (2018).
- [44] Z. H. Liu, X. Y. Xu, Y. Qi, K. Sun, and Z. Y. Meng, Elective-momentum ultrasize quantum Monte Carlo method, *Phys. Rev. B* **99**, 085114 (2019).
- [45] X. Zhang, G. Pan, Y. Zhang, J. Kang, and Z. Y. Meng, Momentum space quantum Monte Carlo on twisted bilayer graphene, *Chin. Phys. Lett.* **38**, 077305 (2021).
- [46] J. S. Hofmann, E. Khalaf, A. Vishwanath, E. Berg, and J. Y. Lee, Fermionic Monte Carlo study of a realistic model of twisted bilayer graphene, [arXiv:2105.12112](https://arxiv.org/abs/2105.12112).
- [47] A. W. Sandvik, Constrained sampling method for analytic continuation, *Phys. Rev. E* **94**, 063308 (2016).
- [48] H. Shao, Y. Q. Qin, S. Capponi, S. Chesi, Z. Y. Meng, and A. W. Sandvik, Nearly Deconfined Spinon Excitations in the Square-Lattice Spin-1/2 Heisenberg Antiferromagnet, *Phys. Rev. X* **7**, 041072 (2017).
- [49] G.-Y. Sun, Y.-C. Wang, C. Fang, Y. Qi, M. Cheng, and Z. Y. Meng, Dynamical Signature of Symmetry Fractionalization in Frustrated Magnets, *Phys. Rev. Lett.* **121**, 077201 (2018).
- [50] N. Ma, G.-Y. Sun, Y.-Z. You, C. Xu, A. Vishwanath, A. W. Sandvik, and Z. Y. Meng, Dynamical signature of fractionalization at a deconfined quantum critical point, *Phys. Rev. B* **98**, 174421 (2018).
- [51] C. Zhou, Z. Yan, H.-Q. Wu, K. Sun, O. A. Starykh, and Z. Y. Meng, Amplitude Mode in Quantum Magnets via Dimensional Crossover, *Phys. Rev. Lett.* **126**, 227201 (2021).
- [52] Z. Yan, Y.-C. Wang, N. Ma, Y. Qi, and Z. Y. Meng, Topological phase transition and single/multi anyon dynamics of Z_2 spin liquid, *npj Quantum Mater.* **6**, 39 (2021).
- [53] Z. Hu, Z. Ma, Y.-D. Liao, H. Li, C. Ma, Y. Cui, Y. Shangguan, Z. Huang, Y. Qi, W. Li *et al.*, Evidence of the Berezinskii-Kosterlitz-Thouless phase in a frustrated magnet, *Nat. Commun.* **11**, 5631 (2020).
- [54] Y. Saito, F. Yang, J. Ge, X. Liu, T. Taniguchi, K. Watanabe, J. I. A. Li, E. Berg, and A. F. Young, Isospin Pomeranchuk effect in twisted bilayer graphene, *Nature (London)* **592**, 220 (2021).
- [55] B. A. Bernevig, Z.-D. Song, N. Regnault, and B. Lian, Twisted bilayer graphene. I. Matrix elements, approximations, perturbation theory, and a $k \cdot p$ two-band model, *Phys. Rev. B* **103**, 205411 (2021).
- [56] Z.-D. Song, B. Lian, N. Regnault, and B. A. Bernevig, Twisted bilayer graphene. II. Stable symmetry anomaly, *Phys. Rev. B* **103**, 205412 (2021).
- [57] B. A. Bernevig, Z.-D. Song, N. Regnault, and B. Lian, Twisted bilayer graphene. III. Interacting Hamiltonian and exact symmetries, *Phys. Rev. B* **103**, 205413 (2021).
- [58] G. Tarnopolsky, A. J. Kruchkov, and A. Vishwanath, Origin of Magic Angles in Twisted Bilayer Graphene, *Phys. Rev. Lett.* **122**, 106405 (2019).
- [59] F. Assaad and H. Evertz, World-line and determinantal quantum Monte Carlo methods for spins, phonons and electrons, in *Computational Many-Particle Physics*, edited by H.

- Fehske, R. Schneider, and A. Weiße (Springer, Berlin, 2008), pp. 277–356.
- [60] Y. Da Liao, Z. Y. Meng, and X. Y. Xu, Valence Bond Orders at Charge Neutrality in a Possible Two-Orbital Extended Hubbard Model for Twisted Bilayer Graphene, *Phys. Rev. Lett.* **123**, 157601 (2019).
- [61] See Supplemental Material at <http://link.aps.org/supplemental/10.1103/PhysRevB.105.L121110> for the momentum-space QMC methodology, the implementation of order measurements within the QMC, and a brief description of the stochastic analytic continuation and exact many-body excitations at the chiral limits.
- [62] O. Vafek and J. Kang, Lattice model for the Coulomb interacting chiral limit of magic-angle twisted bilayer graphene: Symmetries, obstructions, and excitations, *Phys. Rev. B* **104**, 075143 (2021).
- [63] A. W. Sandvik, Stochastic method for analytic continuation of quantum Monte Carlo data, *Phys. Rev. B* **57**, 10287 (1998).
- [64] K. Beach, Identifying the maximum entropy method as a special limit of stochastic analytic continuation, [arXiv:cond-mat/0403055](https://arxiv.org/abs/cond-mat/0403055).
- [65] O. F. Syljuåsen, Using the average spectrum method to extract dynamics from quantum Monte Carlo simulations, *Phys. Rev. B* **78**, 174429 (2008).
- [66] H. Li, Y. D. Liao, B.-B. Chen, X.-T. Zeng, X.-L. Sheng, Y. Qi, Z. Y. Meng, and W. Li, Kosterlitz-Thouless melting of magnetic order in the triangular quantum Ising material TmMgGaO_4 , *Nat. Commun.* **11**, 1111 (2020).
- [67] W. Jiang, Y. Liu, A. Klein, Y. Wang, K. Sun, A. V. Chubukov, and Z. Y. Meng, Pseudogap and superconductivity emerging from quantum magnetic fluctuations: A Monte Carlo study, [arXiv:2105.03639](https://arxiv.org/abs/2105.03639).
- [68] C. Chen, T. Yuan, Y. Qi, and Z. Y. Meng, Fermi arcs and pseudogap in a lattice model of a doped orthogonal metal, *Phys. Rev. B* **103**, 165131 (2021).
- [69] N. N. T. Nam and M. Koshino, Lattice relaxation and energy band modulation in twisted bilayer graphene, *Phys. Rev. B* **96**, 075311 (2017).
- [70] S. Carr, S. Fang, H. C. Po, A. Vishwanath, and E. Kaxiras, Derivation of Wannier orbitals and minimal-basis tight-binding Hamiltonians for twisted bilayer graphene: First-principles approach, *Phys. Rev. Research* **1**, 033072 (2019).
- [71] H. Feldner, Z. Y. Meng, T. C. Lang, F. F. Assaad, S. Wessel, and A. Honecker, Dynamical Signatures of Edge-State Magnetism on Graphene Nanoribbons, *Phys. Rev. Lett.* **106**, 226401 (2011).
- [72] M. Golor, T. C. Lang, and S. Wessel, Quantum Monte Carlo studies of edge magnetism in chiral graphene nanoribbons, *Phys. Rev. B* **87**, 155441 (2013).
- [73] M. Golor, S. Wessel, and M. J. Schmidt, Quantum Nature of Edge Magnetism in Graphene, *Phys. Rev. Lett.* **112**, 046601 (2014).